

Athermal design and analysis for WDM applications

Keith B. Doyle
Optical Research Associates
Westborough, MA

Jeffrey M. Hoffman
Optical Research Associates
Tucson, AZ

ABSTRACT

Telecommunication wavelength division multiplexing systems (WDM) demand high fiber-to-fiber coupling to minimize signal loss and maximize performance. WDM systems, with increasing data rates and narrow channel spacing, must maintain performance over the designated wavelength band and across a wide temperature range. Traditional athermal optical design techniques are coupled with detailed thermo-elastic analyses to develop an athermal optical system under thermal soak conditions for a WDM demultiplexer. The demultiplexer uses a pair of doublets and a reflective Littrow-mounted grating employed in a double-pass configuration to separate nine channels of data from one input fiber into nine output fibers operating over the C-band (1530 to 1561.6 nm). The optical system is achromatized and athermalized over a 0°C to 70°C temperature range. Detailed thermo-elastic analyses are performed via a MSC/NASTRAN finite element model. Finite element derived rigid-body positional errors and optical surface deformations are included in the athermalization process. The effects of thermal gradients on system performance are also evaluated. A sensitivity analysis based on fiber coupling efficiency is performed for radial, axial, and lateral temperature gradients.

Keywords: wavelength division multiplexing, athermal optical design, fiber coupling efficiency, thermo-elastic analysis, integrated modeling, thermal gradients

1. INTRODUCTION

In the field of telecommunications, wavelength-division multiplexing is used in fiber-optic systems to transmit signals at different wavelengths through a single fiber to increase transmission capacity without having to install new fiber. Demultiplexers are used to separate the individual wavelengths from a fiber carrying multiple channels/wavelengths, as shown in Fig. 1.

A wide variety of passive optical components exists to modify and process the optical signals in support of WDM systems including circulators, add-drop devices, routers, couplers, filters, and switches. Many of these components use optical elements to collimate, shape, and direct light from one fiber to another¹. Optical performance in WDM applications may be measured by how well light exiting an optical system couples into an optical fiber, i.e., optical fiber coupling efficiency.

Maintaining high fiber coupling efficiency is critical from a power management standpoint. The optical signal must be strong enough to meet signal-to-noise requirements as well as bit error rates (the fraction of bits transmitted incorrectly). WDM components always exhibit some degree of fiber coupling loss. This loss is determined by the departure of the actual optical system from the ideal optical system as measured by wavefront aberrations and system misalignments². Temperature changes are often responsible for departure from an ideal optical system. Temperature changes cause wavefront error and misalignments by changing the index of refraction, shape, and position of the optical elements. Optical element shape and positional changes result from thermo-elastic contraction and expansion of the optical elements and mounting materials. Higher-order optical surface deformations may occur due to different thermal expansion coefficients between the optics and the mount material and between cemented optical elements.

Thus, the optical design must account for these thermal effects to maintain high coupling efficiency for a successful optical design. The optical system is considered athermal if performance is maintained over a uniform temperature change. This paper discusses the methods to generate an athermal optical design by coupling detailed thermo-elastic effects into the optical design process to provide high fiber coupling efficiency for a WDM demultiplexer. The demultiplexer operates over the telecom C-band (1530-1561.6 nm) and is athermalized from 0°C to 70°C. The optical design uses a pair of doublets and a

reflective Littrow-mounted grating employed in a double-pass configuration. The optical system separates nine channels of data from an SMF-28 input fiber into nine SMF-28 output fibers spaced by 0.25 mm. The fiber coupling efficiency design goal is 90% or greater. A schematic of the demultiplexer is shown in Fig. 2, and system specifications are given in Table 1. The holographic ruled grating has 914.9 lines/mm, which diffracts the central wavelength of 1545.8 nm back upon itself.

Spatial temperature variations provide additional degradation in optical system performance that is typically more severe than thermal soak effects. We performed a sensitivity analysis for fiber coupling efficiency as a function of lateral, axial, and radial gradients for the aforementioned system. Allowable gradients may then be determined based on required system fiber coupling efficiency to guide the design process.

2. OPTICAL FIBER COUPLING EFFICIENCY

Optical fiber coupling efficiency is the percentage of energy that is collected by an optical fiber. The numerical evaluation is performed by computing the overlap integral of the complex PSF and the mode profile of the receiving fiber.

$$CE = \frac{\left| \iint (PSF \bullet \text{mode}) \right|^2}{\iint PSF * PSF^* \bullet \iint \text{mode}^2} \quad (1)$$

Optical aberrations and misalignments of the diffraction image relative to the fiber produce loss in fiber coupling efficiency. Schematics illustrating rigid-body fiber misalignments and wavefront errors are given in Figs. 3 and 4, respectively. We performed a sensitivity study to determine how sensitive fiber coupling efficiency is to misalignments and defocus. This study was performed using the optical design software CODE V^{®3}. The sensitivity analysis assumes that the converging wavefront is spherical with no aberrations present operating at a wavelength of 1550 nm. The optical system numerical aperture was 0.151, and the receiving fiber was a SMF-28 single mode fiber from Corning Glass, Inc. (with a mode field radius of 0.0052 mm at $1/e^2$ intensity).

The first fiber misalignment considered was decenter. Fiber coupling efficiency as a function of fiber decenter is shown in Fig. 5.a. For a coupling efficiency of 90%, the allowable decenter is about 1.4 μm . The single mode profile has a fiber core of 10.4 μm ; thus, this represents a misalignment of over 10% of the diameter.

The second tolerance considered was tilt of the wavefront relative to the fiber. Fiber coupling efficiency as a function of tilt is plotted in Fig. 5.b. For a fiber coupling efficiency of 90%, a tilt of approximately 1.6° is permissible. Since it is more realistic to consider decenter and tilt occurring simultaneously, a set of curves was generated to compare decenter and tilt as a function of fiber coupling efficiency; these are given in Fig. 5.c. Fiber coupling efficiency remains above 90% for a decenter of 1 μm and tilt of 1° . These types of rigid-body errors are common in optical systems with temperature gradients.

Also investigated was the effect of defocus on fiber coupling efficiency. This study is relevant for optical systems that are not athermalized, since uniform temperature changes produces defocus. Approximately 0.23 waves of defocus at 1550 nm cause a loss of 10% in coupling efficiency, as shown in Fig. 5.d.

3. ATHERMALIZATION METHOD

To maintain coupling efficiency over the desired temperature range of 0°C to 70°C and the wavelength band from 1530 to 1561.6 nm, it is necessary to select appropriate lens element materials during optical design to minimize the change in focus position as a function of temperature and wavelength. Athermalization of the lens must take into account the variation in index of refraction with temperature and wavelength, the thermal expansion of the glass and housing materials, mount-induced surface deformations, and potentially, changes in atmospheric pressure.

A useful technique has been described⁴ for selecting glasses for athermalization of multi-lens systems in which the chromatic dispersive power and thermal dispersive power are plotted on a Cartesian coordinate system for each of the prospective glass types (an ‘athermal chart’). For lens element, i , the chromatic dispersive power, ω_i , and thermal dispersive power, θ_i , are

given by Eqns. 1 and 2, where n_i is index of refraction, λ is the central wavelength, $\Delta\lambda$ is the wavelength bandwidth, T is the temperature, and α is the thermal expansion coefficient.

$$\omega_i = -(\partial n_i / \partial \lambda) \Delta\lambda / (n_i - 1) = -1/\text{Abbé No.} \quad (2)$$

$$\theta_i = (\partial n_i / \partial T) / (n_i - 1) - \alpha_i \quad (3)$$

An athermal chart was plotted for the Schott 2000 catalog glasses, after pre-screening for materials with good physical properties. The chart is shown in Fig. 6 for the C-band, with the final glass types selected for the design indicated. The Schott catalog provides equation coefficients for calculation of the change in index of refraction with temperature and wavelength, based on measured data up to 1.06 μm . For calculation of thermal dispersion, we assumed that these equations could be extrapolated to the C-band; the values for dn/dT are listed for each of the selected glasses at temperatures of 0°C, 20°C, and 70°C in Table 2. It is interesting to note that the glass properties are often very different at the C-band than in the visible wavelength range. For example, for the selected design glasses, N-BaF51 behaves as a ‘crown’ glass and SF8 is much more dispersive than SF11.

In Ref. 4, techniques were described for selecting glasses from the chart for thin-lens doublet and triplet designs. With three glass types, the authors concluded that to minimize the individual element powers, it is desirable that the glasses form a triangle with the largest possible inscribed area. As shown in Fig. 6, the glasses selected for the current design fall near the outer boundaries of the dispersion values for all glasses considered, giving a relatively large enclosed area.

During optical design, changes in best focus position and effective focal length of the lens with temperature were calculated using the environmental analysis option in CODE V[®] along with surface deformations and rigid body motions calculated using finite element modeling, as described in Sec. 5. Effects from changes in effective focal length were found to be insignificant for glasses considered for the present design; therefore, the glasses were selected to minimize shift of the best focus position with temperature. The atmospheric pressure was scaled linearly with temperature to model a sealed barrel.

Once a design with good imaging performance is established, to athermalize the lens, it helps to ‘walk’ across the athermal chart for each individual element and observe changes in best focus position, effective focal length, and the optimization error function. Changing to a neighboring glass gives a discontinuous change in best focus position; by choosing the right combination of glasses, the change in focus over a given temperature range (e.g. 0°C to 70°C) can generally be brought close to zero. Once near the solution, adjusting the spacing between doublets and element thickness values help to fine-tune the residual focus shift.

4. OPTICAL DESIGN

For the optical design, a Petzval lens was selected, comprising two positive cemented doublets. The doublets have a standard ‘crown/flint’ configuration, where the positive element is made from low dispersion material, and the negative element is more dispersive. A layout drawing of the optical design is given in Fig. 7, and lens parameters are listed in Table 3. The focal length was selected to give a full image width of 2 mm for the C-band, which allows nine output channels to be used with 0.25 mm spacing and approximately 4 nm separation between wavelengths. The lens parameters given in Table 3 are for a design optimized based on the use of a rigid epoxy for lens mounting (described further in Sec. 5).

For initial optimization, a single pass model was used to balance both odd and even aberrations and to perform glass tradeoffs. Because of symmetry, the odd aberrations tend to cancel in the double-pass configuration, but minimizing them helps to reduce sensitivity to misalignment tolerances, reduces induced aberration terms, and improves imagery for single-pass testing. After finding the single-pass solution, a double-pass model was used for final optimization. Performance of the final design will be discussed below in Sec. 6.

5. DETAILED MECHANICAL ANALYSIS

The nominal optical design was optimized to meet fiber coupling requirements over a 0°C to 70°C uniform temperature range. The CODE V[®] environmental analysis accounted for index of refraction changes with temperature as well as optical element thickness, spacing, and curvature changes due to thermo-elastic effects. Due to the sensitivity of fiber coupling efficiency to positional and wavefront errors in the optical system, a finite element model was developed for the

demultiplexer to more accurately predict the mechanical interaction and to account for additional thermo-elastic effects unaccounted for in the CODE V[®] analysis. These additional effects include higher-order optical surface deformations due to bimaterial bending of the cemented doublets and from mount-induced deformations.

We selected a stainless steel 416 mechanical housing to minimize the expansion/contraction difference between the optical elements and the housing. We assumed that the two doublets were bonded to the housing structure, and we computed mechanical perturbations for two adhesive materials. The first case assumed the doublets were bonded using RTV 566. The thickness of the RTV layer was sized to athermalize the mount. We computed a second set of mechanical perturbations assuming that the doublets were mounted to the housing using Epotek 353ND. This epoxy is much stiffer than the RTV adhesive and is denoted as a ‘rigid’ epoxy due its relative lack of compliance. Material properties for the two bonding materials are shown in Table 4. Flexures were assumed to attach the fused silica grating to the housing and the input and output fibers were assumed mounted in a silicon v-groove array.

A cutaway view of the finite element model is shown in Fig. 8. The model consists of 10,409 elements and 11,195 nodes. The number of nodes representing the optical surfaces of the refractive elements is 217. The number of optical surface nodes for the grating is 587. The material properties are shown in Table 4. Solid finite elements were used to model the optical elements, and plate elements were used to model the housing structure. The distance from the input fiber to the center of the grating is 93.1 mm. The diameter of the first and second doublet (from the fiber plane) is 20 and 24 mm, respectively. Thermal growth is referenced from the input and output optical fiber position, i.e. the fiber plane was constrained in the model. The thermal loading on the model consisted of a 1° thermal soak. The mechanical perturbations were scaled based on the desired temperature assuming a linear response of the mechanical structure over temperature.

The optical surface deformations were fit to Zernike polynomials and applied to the optical model using CODE V[®] surface interferogram files. Optical element rigid-body errors were applied to the optical model using decentered surfaces. The dominant Zernike term is focus for each of the optical element surface deformations. Other terms in the Zernike polynomial representation include spherical aberration and its higher-order forms.

6. SYSTEM PERFORMANCE

As described in Sec. 5, an initial design was performed using surface deformations based on the use of an RTV adhesive sized to athermalize the mount. Under this assumption, the surface deformations were found to give a negligible change in coupling efficiency (within 0.2%) compared with the performance excluding mount-induced surface deformations. The coupling efficiency performance achieved is given in Fig. 9.a., showing that the performance goal of 90% coupling efficiency was easily met, with more than 95% coupling efficiency achieved over the full C-band from 0°C to 70°C.

However, if a rigid epoxy is used, the resulting surface deformations result in significant degradation of performance. Figure 9.b. shows the coupling efficiency if the lens design is not adjusted to compensate for mount-induced deformations. As shown, the coupling efficiency at 70°C drops to 86% at the shortest wavelength, which is below the 90% specification.

For the final design, the lens parameters were adjusted to balance the effects of the mount-induced surface deformation using a rigid epoxy, giving more than 95.5% coupling efficiency over the operating wavelength and temperature ranges, as shown in Fig. 9.c.

In Fig. 9.d., the shift of the best composite focus position with temperature is plotted for each of these cases from 0°C to 70°C. The initial design using athermally-sized RTV has a maximum focus shift range of 1.5 μm . Using rigid epoxy without reoptimizing the lens gives a focus range of 35.3 μm , which is reduced to 1.6 μm after compensation.

7. THERMAL GRADIENT ANALYSIS

We also investigated the effects of thermal gradients in the demultiplexer system on fiber coupling efficiency. External and internal heat sources may produce spatially varying temperatures in the optical instrument, which would degrade optical system performance. The goal was to set thermal design and control limits by determining the maximum allowable lateral, axial, and radial gradients. We computed optical element rigid-body motions and surface deformations for unit gradients in the lateral, axial, and radial directions using the thermo-elastic displacement quantities generated by the finite element model using the RTV adhesive to mount the optical elements.

Optical element rigid-body motions were applied to the CODE V[®] model by decentering and tilting the individual surfaces, and optical surface deformations were fit to Zernike polynomials and applied using surface interferogram files. Thermo-optic finite element models were generated for the refractive optical elements; these models approximate the effects on wavefront error due to changes in the index of refraction with temperature. This technique substitutes the thermo-optic coefficient in place of the coefficient of thermal expansion on the material card definition in the finite element model while applying the necessary boundary conditions.

The gradient-generated perturbations were linearly scaled, and coupling efficiency was computed as a function of the magnitude of the temperature gradient. The temperature distributions are shown on the finite element model in Figs. 10 to 12. The most severe effect is due to the lateral gradient, which induces asymmetrical effects, including optical element decenters and tilts. The gradient curves indicate that a 10% loss in fiber coupling is produced for a 0.21°C lateral gradient, 1.8°C axial gradient, and a 2.1°C radial gradient. A combined effect of the gradients was not investigated.

8. SUMMARY

Athermalization techniques were employed to design and analyze the performance of a wavelength demultiplexer for telecommunication systems as a function of temperature. The optical system consists of two doublets and a diffraction grating operating in a double-pass configuration. One input fiber carries nine channels of data that are separated by the demultiplexer into nine output fibers. Traditional optical design athermalization methods were coupled with finite-element-derived thermo-elastic computations to optimize the optical design over the operating temperature range (0°C to 70°C).

The final optical design was based on an iterative process. An initial optical design was generated using the environmental module of CODE V[®] to optimize performance based on index changes with temperature as well as positional and shape changes in the optical surfaces due to thermal expansion. A MSC/NASTRAN finite element model was developed to compute more accurate changes in the position and shape of the optical elements by taking into account the specific optical element to housing interface as well as accounting for the bi-material bending of the two doublets. These additional perturbations were included in the optical model, and fiber coupling efficiency was computed for the nine output fibers over temperature.

This effort was performed for two different bonding materials: an athermally-sized RTV adhesive and a rigid epoxy. The change in coupling efficiency, prior to re-optimizing, was approximately 1% with the inclusion of the mechanical perturbations using the RTV bond. The addition of the perturbations from the rigid epoxy caused a maximum drop in system coupling efficiency of approximately 9%.

With re-optimization of the optical design, the fiber coupling efficiency exceeded the design goal of 90% for all fibers over the full 0°C to 70°C temperature range. The sensitivity of fiber coupling efficiency to thermal gradients was also computed. The analysis showed that to maintain fiber coupling efficiency above 90% for each output fiber, the lateral gradient must be kept to 0.21°C or less. For axial and radial gradients, a fiber coupling efficiency of 90% is met for temperatures gradients of 1.8°C and 2.1°C, respectively. The thermal gradient temperature sensitivity study did not consider the effects of combinations of types of gradients.

REFERENCES

1. W. Tomlinson, "Wavelength multiplexing in multimode optical fibers," *Appl. Optics*, Vol. 16, No. 8, August 1977.
2. R. Wagner and W. Tomlinson, "Coupling efficiency of optics in single-mode fiber components," *Appl. Optics*, Vol. 21, No. 15, August 1982.
3. CODE V[®] Reference Manual, Optical Research Associates, 3280 East Foothill Boulevard, Pasadena, CA.
4. Y. Tamagawa, S. Wakabayashi, T. Tajime, and T. Hashimoto, "Multilens system design with an athermal chart," *Appl. Optics*, Vol. 33, No. 34, December 1994.

TABLES

Parameter	Specification
1. System Configuration	Double pass with input fiber, lens group, grating, and nine output fibers
2. Optical Source	
i. Type	Laser Diode
ii. Power (mW)	0.1
iii. Center Wavelengths Span (nm)	1530-1561.6
iv. Channels	9
v. Separation (nm)	4.0
vi. Line Bandwidths	Assumed zero
3. Input Fiber	
i. Optical Fiber Type	Corning SMF-28
ii. Diameter at $1/e^2$ Intensity (μm)	10.4
iii. Numerical Aperture at 99% Power Pt.	0.151
iv. Gaussian Radius relative to pupil ($1/e^2$)	0.649
v. Fiber Position (mm)	(X,Y) = 0.125, 0
4. Grating	
i. Type	Holographic/Ruled
ii. Order	-1
iii. Period	914.9 lines/mm
5. Output Fibers	
i. Optical Fiber Type	Corning SMF-28
ii. Fiber Positions (mm)	(X,Y) = (-0.125, 1.014) to (-0.125, -0.986) over C-band, spaced by 0.25
6. Optical System	
i. Effective Focal Length (mm)	48.9 at $\lambda = 1545.8 \text{ nm}$
ii. Field of View (degrees)	± 1.17
7. Coupling Efficiency	> 90% GOAL
8. Housing Material	416 Stainless Steel
9. Optical Axis Length (mm)	< 100
10. Operational Temperature Range ($^{\circ}\text{C}$)	0 to 70

Table 1. Optical System Specifications

Material	n	dn/dT ($\times 10^6$)		
		T = 0 $^{\circ}\text{C}$	T = 20 $^{\circ}\text{C}$	T = 70 $^{\circ}\text{C}$
SF11	1.744805	6.932	7.336	8.039
N-BaK1	1.555247	-0.045	0.185	0.708
N-SF8	1.657277	-0.828	-0.628	-0.257
N-BaF51	1.629404	0.008	0.215	0.639

Table 2. Index of Refraction and dn/dT at 0, 20, and 70 $^{\circ}\text{C}$ and $\lambda = 1545.98 \text{ nm}$

Surface	Radius of Curvature (mm)	Thickness (mm)	Material
Input	---	16.875	---
Doublet 1, Surface 1	Plano	8.5	SF11
Doublet 1, Surface 2	21.52	6.5	N-BaK1
Doublet 1, Surface 3	-21.52	29.745	Air
Doublet 2, Surface 1	-60.32	5	N-SF8
Doublet 2, Surface 2	21.52	7	N-BaF51
Doublet 2, Surface 3	-30.37	20	Air
Grating (Stop)	Plano	0	---

Table 3. Lens Surface Data from Input Fiber to Grating (used in double pass). The design is athermalized assuming the use of rigid epoxy for lens mounting.

Material Properties			
Material	Elastic Modulus (KN/mm ²)	Poisson Ratio	CTE (ppm/°C)
SF11	66	0.24	6.1
N-BaK1	73	0.25	7.6
N-SF8	88	0.25	8.6
N-BaF51	91	0.26	8.4
Fused Silica	72	0.17	0.5
SS416	215	0.28	9.9
RTV 566	0.004	0.45	230
353ND	3.0	0.38	60

Table 4. Mechanical Properties

FIGURES

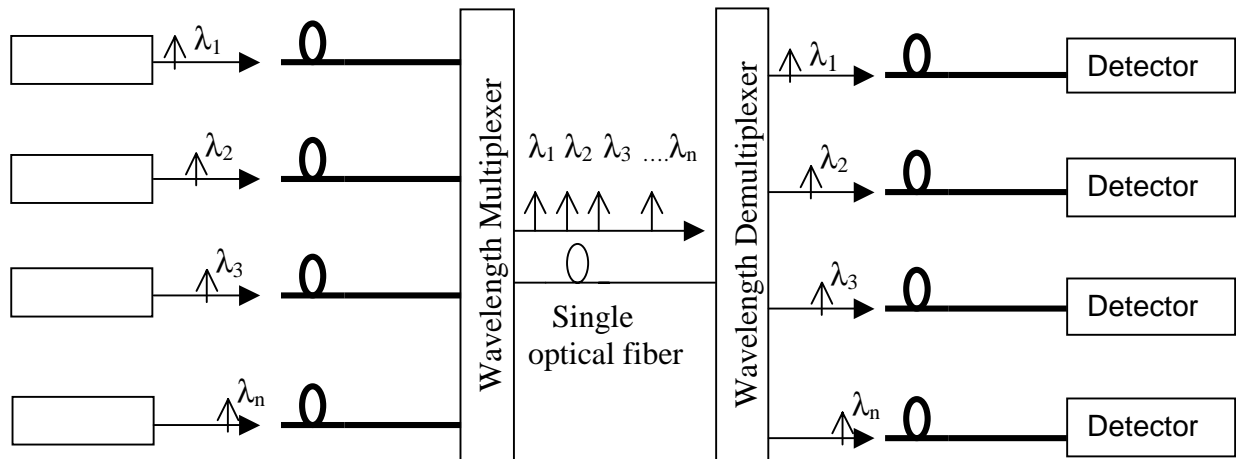


Figure 1. Wavelength Division Multiplexing Schematic

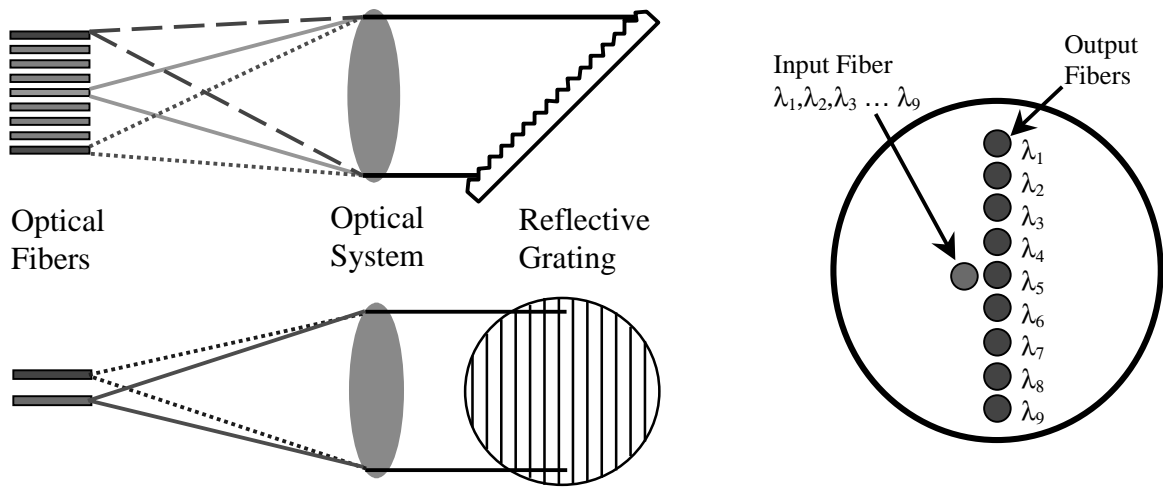


Figure 2. WDM Demultiplexer

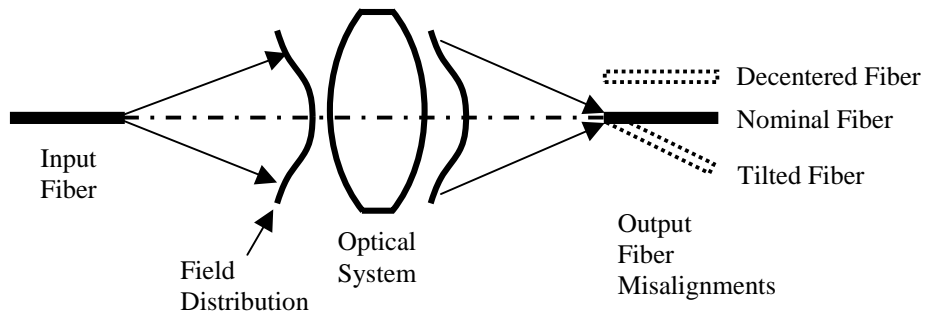


Figure 3. Rigid-Body Fiber Misalignments

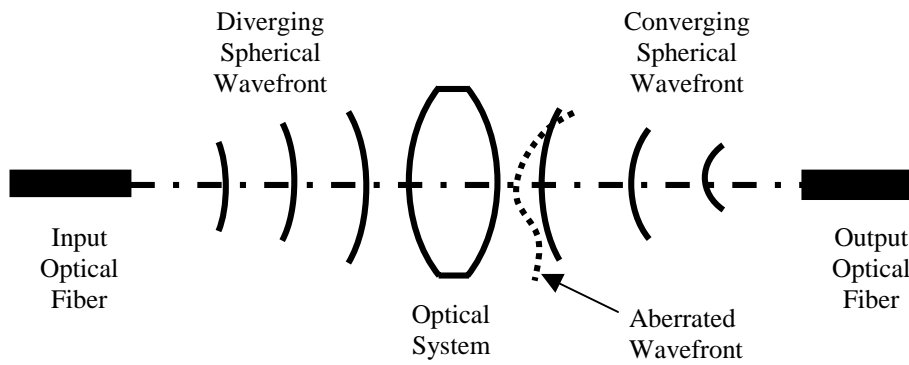


Figure 4. Wavefront Errors in Optical System

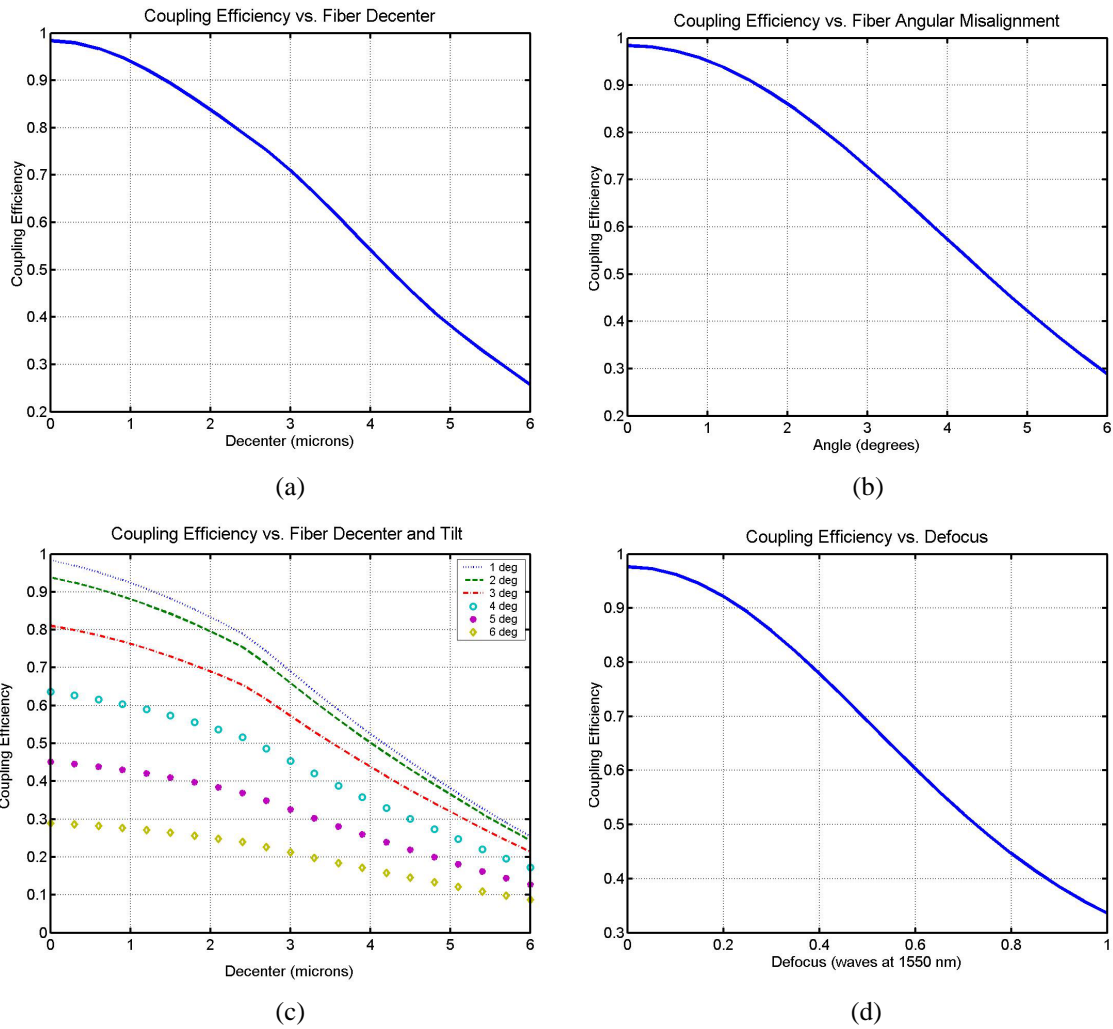


Figure 5. Fiber Coupling Efficiency vs. Fiber Misalignments and Focus Error

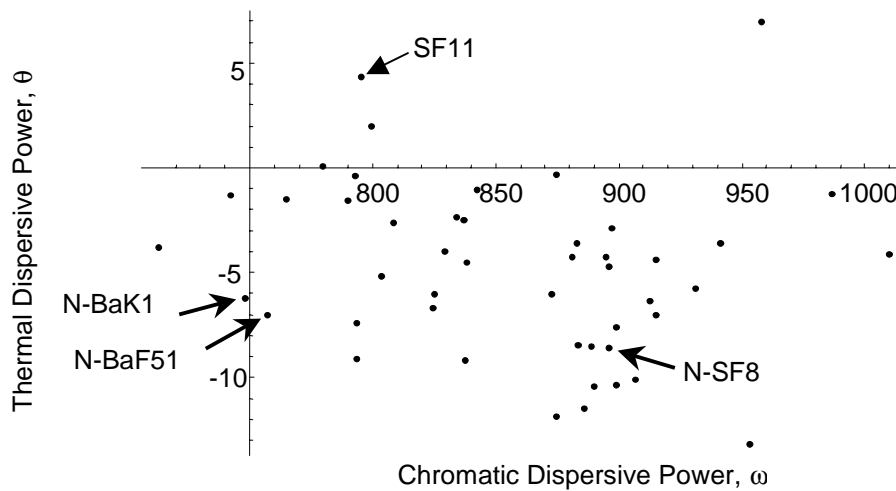


Figure 6. Thermal versus chromatic dispersive power for selected Schott 2000 catalog glasses at the C-band for use in lens athermalization. Final glass selections are indicated.

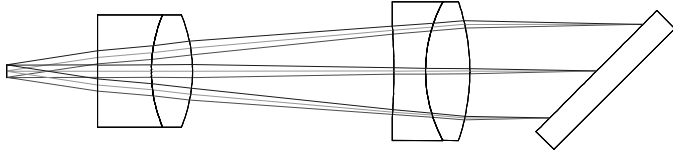


Figure 7. Demultiplexer CODE V Double-Pass Optical Model

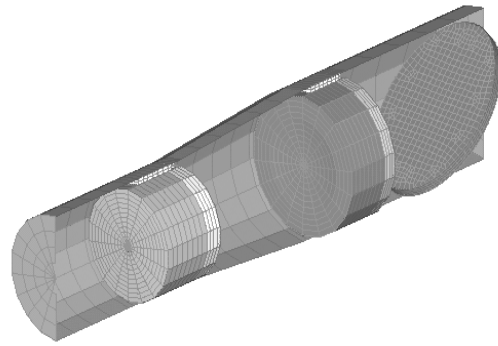
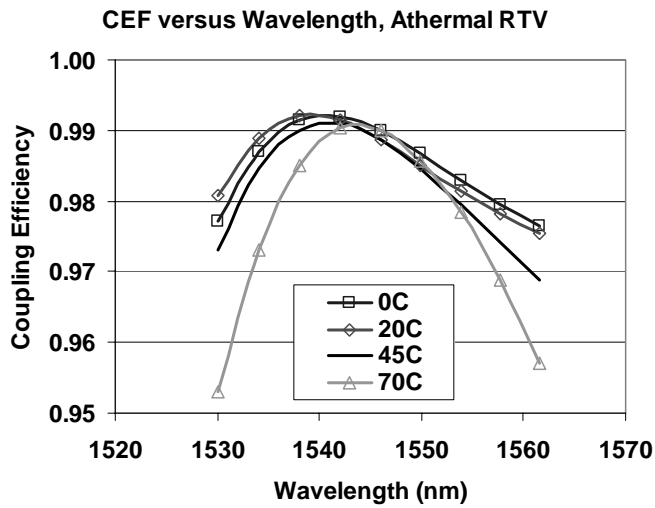
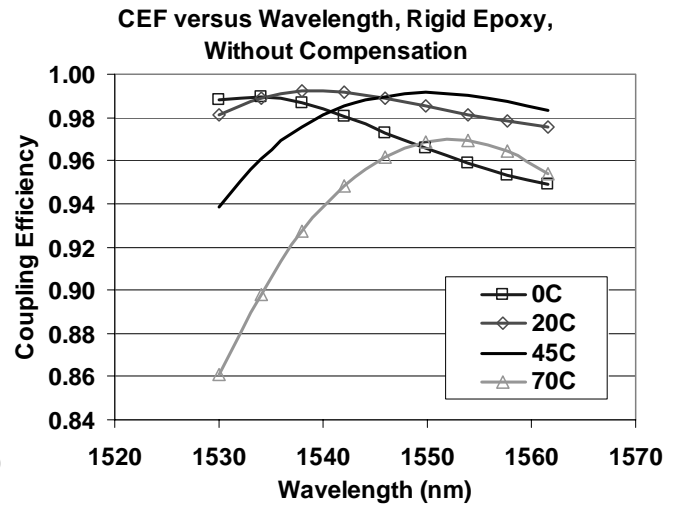


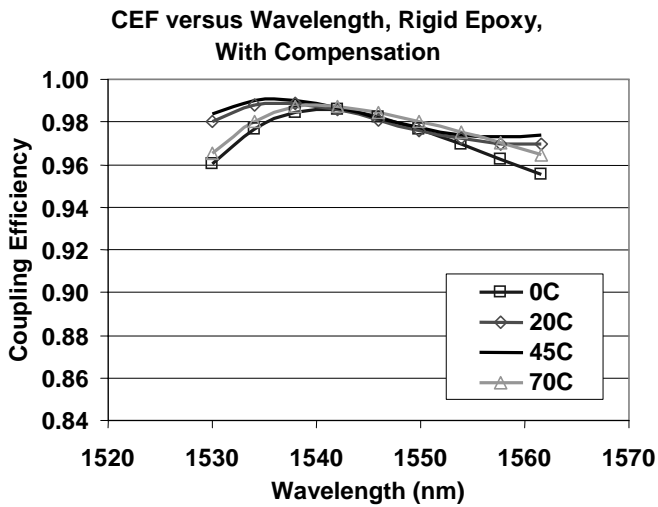
Figure 8. Demultiplexer Finite Element Model



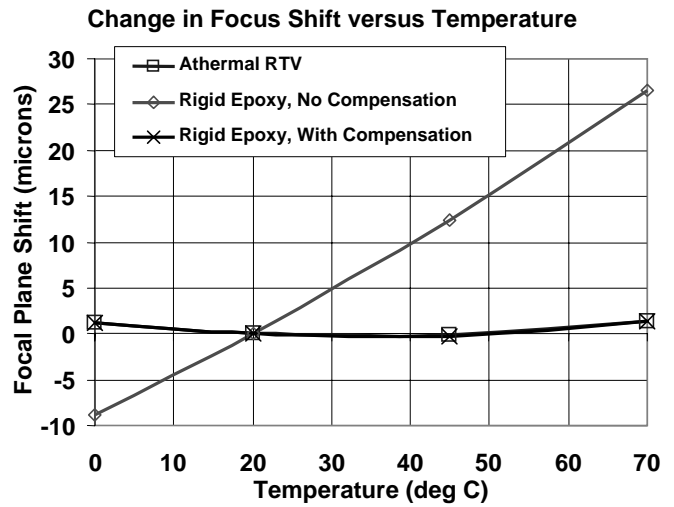
(a)



(b)



(c)



(d)

Figure 9. Coupling Efficiency and Focus Shift with Athermal RTV and Rigid Body Epoxy Lens Mounting

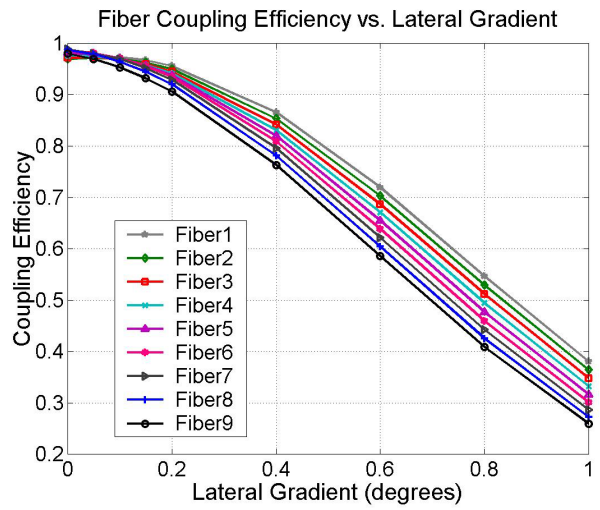
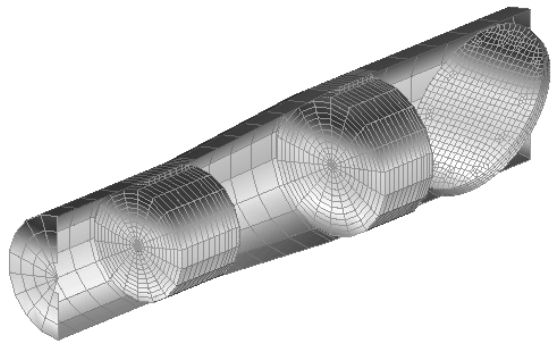


Figure 10. Fiber Coupling Efficiency vs. Lateral Temperature Gradient

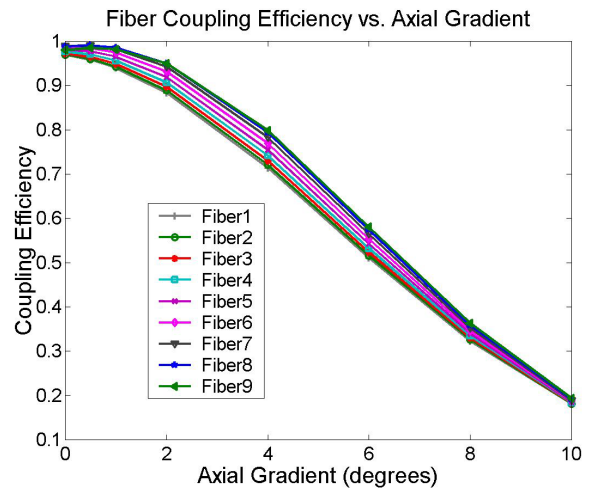
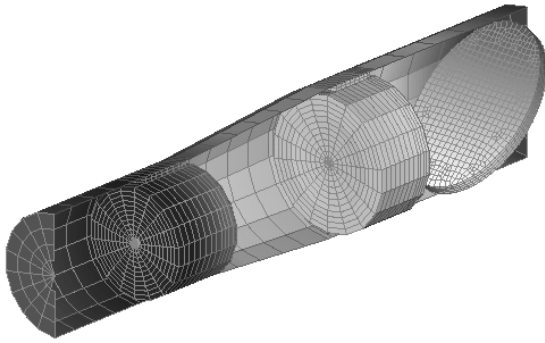


Figure 11. Fiber Coupling Efficiency vs. Axial Temperature Gradient

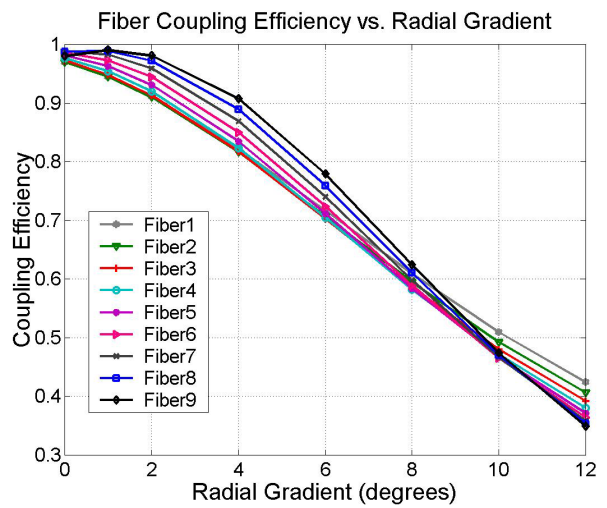
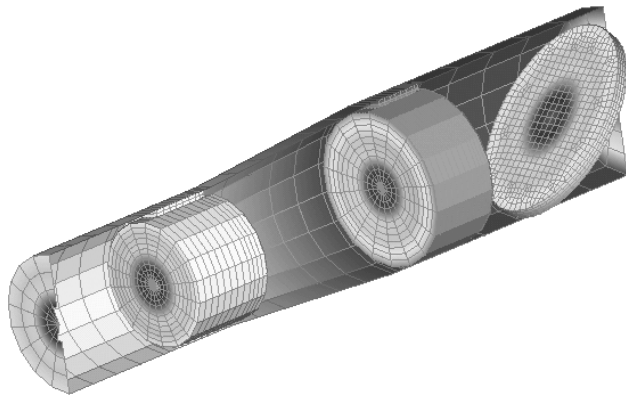


Figure 12. Fiber Coupling Efficiency vs. Radial Temperature Gradient